bioRxiv preprint doi: https://doi.org/10.1101/2021.02.17.431682; this version posted February 17, 2021. The copyright holder for this preprint (which was not certified by peer review) is the author/funder. All rights reserved. No reuse allowed without permission.

Mechanical stress determines morphogenesis and cell ordering in confined bacterial biofilms

Qiuting Zhang[1], Jian Li[3], Japinder Nijjer[1], Haoran Lu[1], Mrityunjay Kothari[3], Ricard Alert[4,5], Tal Cohen[2,3,]*, Jing Yan[1,6,]*.

[1] Department of Molecular, Cellular and Developmental Biology, Yale University, New Haven, CT 06511, USA.
[2] Department of Mechanical Engineering, Massachusetts Institute of Technology, Cambridge, MA 02139, USA.
[3] Department of Civil and Environmental Engineering, Massachusetts Institute of Technology, Cambridge, MA 02139, USA.
[4] Princeton Center for Theoretical Science, Princeton University, Princeton, NJ 08544, USA
[5] Lewis-Sigler Institute for Integrative Genomics, Princeton University, Princeton, NJ 08544, USA
[6] Quantitative Biology Institute, Yale University, New Haven, CT 06511, USA.

* To whom correspondence should be addressed. E-mail: talco@mit.edu and jing.yan@yale.edu.

Abstract:

Biofilms are aggregates of bacterial cells surrounded by an extracellular matrix. Much progress has been made in studying biofilm growth on solid substrates; however, little is known about how biofilms develop in three-dimensional confined environments. Here, combining single-cell imaging, continuum mechanical modeling, and mutagenesis, we reveal the key morphogenesis steps of *Vibrio cholerae* biofilms embedded in hydrogels. We demonstrate how mechanical stress determines the global morphology and gives rise to bipolar cell ordering in confined biofilms. Our analysis shows that cell ordering arises from stress transmission across the biofilm-environment interface, mediated by specific matrix components. Our results open an avenue to understand how organisms grow within complex environments by means of a compromise between their inherent developmental program and the constraints imposed by the environment.

One sentence summary: Embedded biofilms mechanically interact with the confining environment, leading to the emergence of an anisotropic architecture and a precise cell organization.

Main Text:

The growth of living organisms is critically influenced by the external environment. One form of such environmental influence is the transmission of mechanical stress, which can instruct morphogenesis in systems ranging from stem cells to tissues to entire organisms (*1–3*). In the prokaryotic domain, bacteria commonly live in complex communities encased by an extracellular matrix (*4*), known as biofilms (*5*). Biofilm formation is a morphogenetic process whereby a single founder cell develops into a three-dimensional aggregate in which bacterial cells interact with each other and with the environment (*5–7*). Recent work has revealed biophysical mechanisms underlying biofilm morphogenesis on solid substrates, which is controlled by cell-substrate adhesion and the resulting shear stress (*8–10*). In addition to those living on surfaces, bacterial communities are also commonly found inside soft, structured environments such as hydrogels. Examples include biofilms growing in mucus layers and host tissues during an infection or food contamination. Indeed, many common biofilm formers

bioRxiv preprint doi: https://doi.org/10.1101/2021.02.17.431682; this version posted February 17, 2021. The copyright holder for this preprint (which was not certified by peer review) is the author/funder. All rights reserved. No reuse allowed without permission.

including *Pseudomonas aeruginosa* and *Vibrio cholerae* encounter biological hydrogels as their niche during infection (*11*, *12*). Under these conditions, cells must grow against three-dimensional (3D) mechanical confinement. However, little is known about how biofilms develop under such mechanical constraints, including how cells collectively organize in response to the confinement and how the confining environment, in turn, is modified by cell proliferation. This is in stark contrast to the accumulating knowledge on the growth dynamics of mammalian cell aggregates and tumors under confinement (*13*, *14*).

In this study, we integrate single-cell live imaging, mutagenesis, *in vitro* mechanical testing, and numerical modeling to investigate how cells in embedded biofilms mechanically communicate with each other and with the environment. A model system is established by embedding *V. cholerae*, the causal agent of the cholera pandemic and a model biofilm former (*15*, *16*), inside agarose gels. By using 3D visualization techniques with high spatiotemporal resolution, we reveal that embedded biofilms undergo shape transition and a series of self-organization events that are distinct from those in surface-attached biofilms. We show that the overall biofilm morphology results from growth-induced stresses that depend on the stiffness contrast between the biofilm and the confining hydrogels. Furthermore, we discover that embedded biofilms display a core-shell structure with intricate ordering similar to nematic liquid crystal droplets (*17*). Finally, we demonstrate that Vibrio polysaccharide (VPS) and cell-to-surface adhesion proteins effectively transmit stress from the environment to the biofilm, giving rise to distinct cell ordering patterns in embedded biofilms.

Single-cell imaging reveals distinct growth pattern of embedded *V. cholerae* biofilms

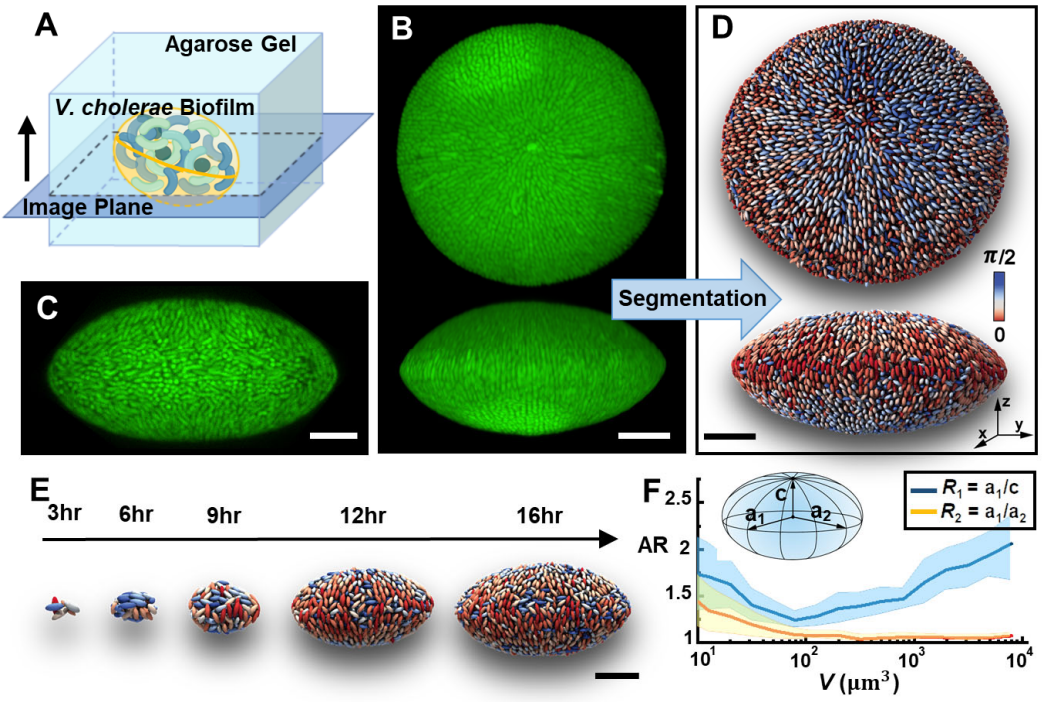

bioRxiv preprint doi: https://doi.org/10.1101/2021.02.17.431682; this version posted February 17, 2021. The copyright holder for this preprint (which was not certified by peer review) is the author/funder. All rights reserved. No reuse allowed without permission.

Figure 1. Single-cell imaging of embedded *V. cholerae* biofilms. (**A**) Schematic illustration of biofilm growth in agarose gels. (**B**) 3D view (top and side) and (**C**) cross-sectional image of a *V. cholerae* biofilm from Δ*rbmA* mutant cells embedded in a 2% agarose gel. Cells constitutively express mNeonGreen. Scale bar: 10 μm. (**D**) Single-cell 3D reconstruction of the embedded biofilm shown in **B**. Cells are color-coded according to their angles with respect to the *z* axis. (**E**) Time-lapse images of reconstructed biofilms. Scale bar: 5 μm. (**F**) Evolution of biofilm morphology inside 2% agarose gel characterized by two aspect ratios (ARs) as a function of biovolume *V*. Inset shows the definition of aspect ratios $R_1 = a_1/c$ and $R_2 = a_1/a_2$, in which $a_1, a_2,$ and c $(a_1 > a_2 > c)$ are the biofilm's principal axes. Center lines correspond to means; widths of the shaded areas correspond to standard deviation (SDs, $n = 10$).

A convenient agarose-based assay is developed to investigate the interplay between biofilm growth and mechanical confinement: individual cells are embedded at low density and allowed to grow into isolated biofilm clusters inside agarose gels of varying stiffnesses controlled by the agarose concentration (**Fig. 1A** and fig. S1) (*18*). This growth geometry is widely used in bacteriophage assay (*19*). The biocompatibility and tunable mechanical properties render agarose gels a suitable embedding medium to grow biofilms without affecting the growth rate of the encapsulated cells (fig. S2). We use the well-characterized rugose (Rg) *V. cholerae* strain locked in a high cyclic diguanylate level to focus on the biomechanical aspect of biofilm growth (*9*, *20*). We start with a mutant lacking the cell-to-cell adhesion protein RbmA, as the surface-attached biofilm from this mutant is best understood (*8*, *10*, *21*). To quantitatively track the architecture of growing biofilms, we adopt an adaptive imaging technique to obtain microscopy data with high spatiotemporal resolution over the full course of biofilm growth (*9*). We are able to visualize both the global morphology and the single-cell level architecture of an embedded biofilm containing up to 10^4 cells (**Fig. 1, B and C**, movie S1) with minimal phototoxicity and photobleaching. In parallel, we develop an adaptive local thresholding algorithm to segment individual cells in 3D confined biofilms with minimal segmentation error (**Fig. 1D** and fig. S3, movie S2). This new algorithm overcomes the issue of image deterioration due to dense cellular packing and light scattering, both of which are significant for embedded biofilms. Our technique enables the first single-cell view of biofilm architecture away from a glass substrate.

Both on global and single-cell levels, mature embedded biofilms possess a 3D organization distinct from that in biofilms growing on solid substrates. At the global level, the entire biofilm develops an anisotropic oblate shape. This is unexpected because previous results showed that free-floating biofilm clusters are roughly spherical (*9*). At the single-cell level, embedded biofilms display a precise pattern of nematic cell alignment: at the biofilm-gel interface, the rod-shaped *V. cholerae* cells align radially around the two poles of the biofilm. In the language of liquid crystals (LCs), the two poles correspond to +1 defects around which the local alignment axis rotates by 360° (*22*). The observed configuration is reminiscent of the bipolar organization of LC molecules on the surface of droplets, with the two +1 defects known as Boojum points (*17*).

Our imaging pipeline also reveals the key developmental stages of embedded biofilms. We follow the growth of well-separated biofilms from single founder cells to mature clusters at a time resolution of one cell division cycle (fig. S4 and movie S3). The reconstructed data at

bioRxiv preprint doi: https://doi.org/10.1101/2021.02.17.431682; this version posted February 17, 2021. The copyright holder for this preprint (which was not certified by peer review) is the author/funder. All rights reserved. No reuse allowed without permission.

single-cell resolution (**Fig. 1E**) show that, initially, small clusters are elongated due to the inherent shape anisotropy of the founder cell and the subsequent division along its long axis. At the early stage, embedded biofilms tend to grow from a prolate (R_1>R_2 >1, **Fig. 1F**) to a close-to-spherical shape (R_1~R_2~1). However, as the biofilm keeps growing, the spherical shape gradually transforms into an oblate shape (R_1>R_2 =1). Concomitantly, cells at the biofilm-gel interface develop the bipolar nematic order described above. The non-monotonic biofilm shape evolution and the bipolar cell ordering pose a central question: *How does mechanical confinement impact biofilm growth and architecture both at global and local levels?*

The biofilm-environment stiffness contrast determines biofilm morphology

We hypothesize that the anisotropic biofilm shapes result from the accumulation of growth-induced mechanical stresses under the constraints imposed by the environment. The biofilm-environment interaction is bidirectional: Cell proliferation generates stress and deforms the confining environment, which, in turn, affects the biofilm morphology and the cell organization. To quantitate this two-way interaction, we measure the evolution of the major aspect ratio R_1 of biofilms subjected to different degrees of confinement by tuning agarose stiffness (**Fig. 2A**). We find that the morphological evolution depends strongly on the degree of confinement: when the gel concentration is low (≤0.5%), the biofilm grows towards a spherical shape and stays spherical. In contrast, biofilms in stiffer hydrogels undergo a prolate-to-spherical-to-oblate transition and mature biofilms maintain an oblate shape.

We envision that embedded biofilm growth bears conceptual similarity with the classical problem of elastic cavitation, i.e. the expansion of fluid cavity inside an elastic material (*23–25*). However, unlike liquid inclusions, the biofilm behaves as a viscoelastic and poroelastic solid (fig. S5); it resists deformations imposed by the confining environment to some extent. Therefore, embedded biofilm growth can be conceptualized as a *solid inclusion* expanding inside another *solid*. The mechanical properties of the biofilm and the agarose gel can be characterized by their shear moduli, G_b and G_a (tables S1 and S2), respectively. We vary the stiffness of a biofilm by using different mutants lacking one or more extracellular matrix components (*26*). We measure the average aspect ratio of mature biofilms (~10^4 μm^3) for different stiffness contrasts between the biofilm and the embedding hydrogel, G_b/G_a (**Fig. 2B**). The resulting diagram shows that the anisotropic biofilm morphology is favored when the environment is stiffer than the embedded biofilm (G_b/G_a < 1, **Fig. 2B**).

bioRxiv preprint doi: https://doi.org/10.1101/2021.02.17.431682; this version posted February 17, 2021. The copyright holder for this preprint (which was not certified by peer review) is the author/funder. All rights reserved. No reuse allowed without permission.

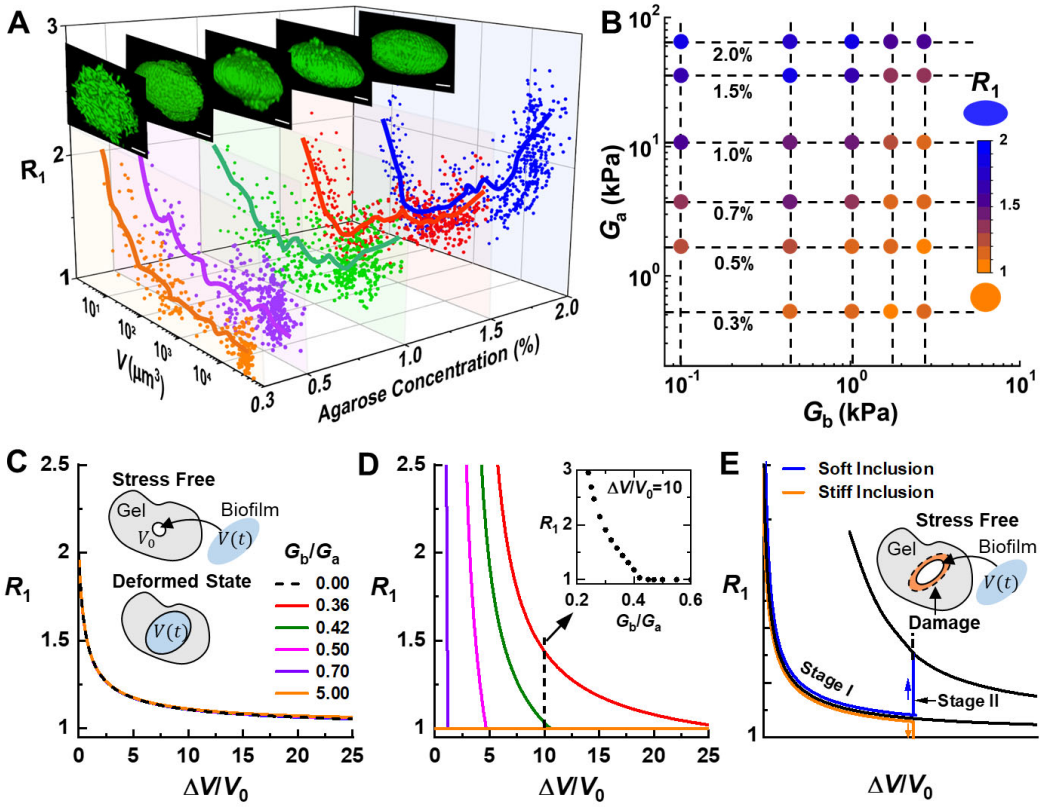

Figure 2. Stiffness contrast determines biofilm shape anisotropy. (**A**) Morphologies of biofilms from Δ*rbmA* cells growing in hydrogels solidified with different concentrations of agarose. Plotted are the biofilm aspect ratio R_1 versus V obtained at different developmental stages. Solid lines are running means of the data points. Insets show images of representative biofilms for each condition. Scale bar: 5 μm. (**B**) Diagram showing biofilm shape as a function of biofilm stiffness G_b and agarose gel stiffness G_a. Symbols are color-coded according to the average R_1 of mature biofilms, ranging from 1 (spherical) to 2 (oblate). (**C-E**) Theoretical modeling examines R_1 variation as a function of the volumetric expansion ratio ($\Delta V/V_0$) for different stiffness contrasts G_b/G_a and at different stages of expansion. V_0 corresponds to initial void volume and $\Delta V = V - V_0$. (**C**) Stage I – purely elastic deformation of the gel without any damage. Insets illustrate the modeling approach to determine the optimal biofilm shape. (**D**) Stage II – onset of damage in the gel environment. Inset shows that at a fixed volumetric ratio $\Delta V/V_0$, R_1 decreases with increasing stiffness contrast G_b/G_a, qualitatively capturing the experimental observations in **B**. (**E**) Schematic explanation of the shape evolution of embedded biofilms: In Stage I, the gel deforms elastically, and R_1 evolves toward 1 for both soft and stiff inclusions (biofilms), similar to the expansion of a fluid cavity. After gel damage (indicated by the orange region) occurs in Stage II, R_1 increases for soft inclusions but drops to 1 for stiff inclusions.

Continuum modeling of inclusion growth reveals that gel damage causes a transition in biofilm morphology

The oblate biofilm shape is reminiscent of macroscopic penny-shaped cracks commonly observed in brittle materials (*24*). However, hydrogel labeling experiments show the absence of crack (fig. S6) and a scaling analysis (*27*) indicates that the embedded biofilms in

bioRxiv preprint doi: https://doi.org/10.1101/2021.02.17.431682; this version posted February 17, 2021. The copyright holder for this preprint (which was not certified by peer review) is the author/funder. All rights reserved. No reuse allowed without permission.

this study are too small to generate macroscopic cracks (table S3). To explain the observed biofilm shape evolution in the absence of crack, we develop a continuum model that couples biofilm growth with the nonlinear mechanical response of the environment (*28*). We model the biofilm as a solid inclusion constrained to fit into a void in an infinite elastic medium, with biofilm growth driving void expansion (**Fig. 2C, inset**, fig. S7-9). If the biofilm were not subject to the confinement, it would develop a random organization resulting from cell proliferation in all directions (*9*) (fig. S10). This indicates the absence of an inherent, programmed morphology in growing biofilms, in contrast to higher-order organisms. Hence, the key factor in determining biofilm shape is the accumulation of mechanical energy imposed by the external constraint. Specifically, we hypothesize that an embedded biofilm will evolve in a way to minimize the total mechanical energy in the system. This energy minimization yields an optimal shape of the confined biofilm at every given volume; this optimal shape is different from the stress-free shapes of both the void and the biofilm.

Given that the surrounding material endures large strains, we propose two growth stages. In Stage I (**Fig. 2C**), the confining gel deforms elastically so that the stress-free shape of the void is preserved while the biofilm is allowed to vary its stress-free shape. Our calculations show that in this stage the optimal R_1 quickly decreases to 1 regardless of the stiffness contrast G_b/G_a – a situation similar to the classical problem of fluid cavity expansion. In Stage II, the strain generated by biofilm growth exceeds the elastic limit of the gel material in the region immediately surrounding the biofilm – damage thus occurs (*27*). Accordingly, the void can no longer maintain its original stress-free shape and we assume that the void's stress-free shape now varies with that of the growing biofilm (**Fig. 2D**). Therefore, we predict that the biofilm adopts a new optimal shape at the onset of damage. This hypothesis is corroborated by our experiments showing that the volume at which the shape transition takes place scales with the maximum deformation the gel can sustain (**Fig. 2A** and fig. S11). It should be noted that the observed experimental transitions are expected to be gradual due to multiple relaxation processes in both the biofilm and the environment. Interestingly, this transition strongly depends on G_b/G_a (**Fig. 2D, inset**). Combining the results of Stage I and II, we interpret the full evolution of biofilm shape (**Fig. 2E**). Starting from an elongated shape, an embedded biofilm initially evolves toward a spherical shape as if it were a fluid (Stage I); upon the onset of gel damage (Stage II), a biofilm stiffer than its environment will become even more spherical, while a biofilm softer than the environment will transition to an oblate shape.

bioRxiv preprint doi: https://doi.org/10.1101/2021.02.17.431682; this version posted February 17, 2021. The copyright holder for this preprint (which was not certified by peer review) is the author/funder. All rights reserved. No reuse allowed without permission.

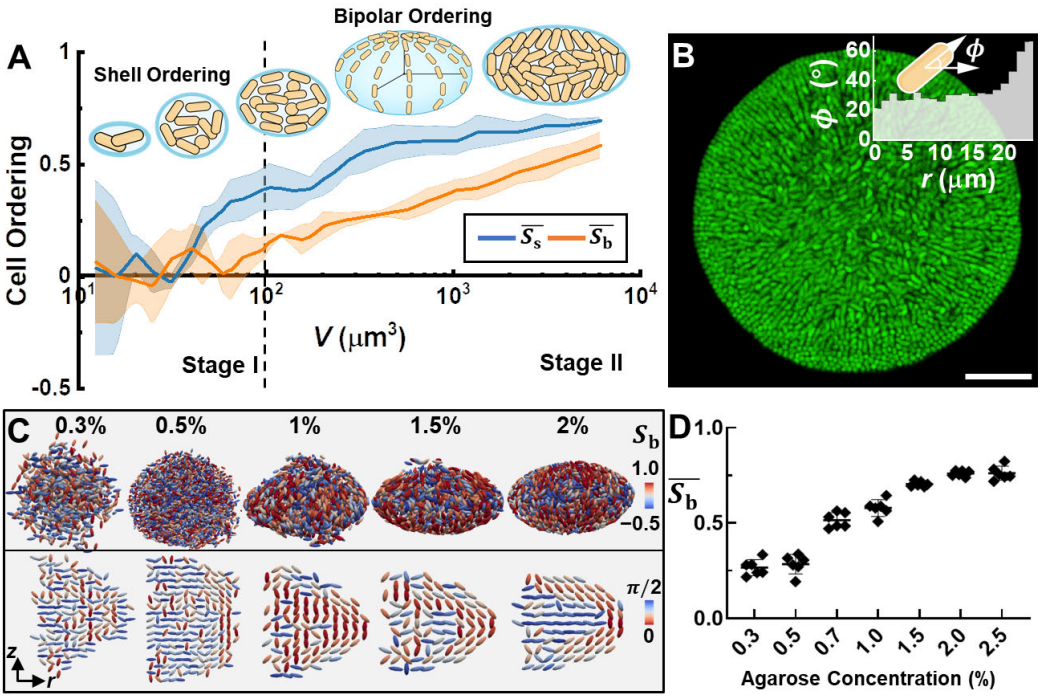

Figure 3. Cell ordering is promoted by biofilm-gel mechanical interactions. (**A**) Evolution of cell ordering with biovolume V for a biofilm in 2% gel. Cell ordering is quantified by the average shell ordering $\overline{S_s}$ and average bipolar ordering $\overline{S_b}$ in the outmost cell layers. Center lines correspond to means; widths of the shaded areas correspond to SDs (n = 3). Inset: Schematic representation of the development of biofilm architecture. (**B**) Cross-sectional view of the principal plane of a mature biofilm. Inset: Average angle ϕ between a cell's axis and the biofilm's principal plane as a function of the distance from the center r. Scale bar: 10 μm. (**C**) Architecture of mature biofilms inside gels of designated agarose concentrations. Shown are the 3D reconstructed biofilms with each cell colored according to its bipolar order parameter S_b (*Top*) and average angle between the cell axis and the z axis (*Bottom*, see fig. S12). (**E**) Average bipolar order parameter $\overline{S_b}$ of mature biofilms grown in agarose gels with the designated concentrations. Error bars correspond to SDs (n = 7).

Bacterial cells self-organize as embedded biofilms grow

As shown in **Fig. 1**, cells at the biofilm-gel interface self-organize into an ordered pattern under confinement. To quantify cell ordering, we employ established tools in LCs (*22*). We measure cell orientation with respect to the biofilm-gel interface to define two orthogonal order parameters (fig. S12): the shell order parameter S_s and the bipolar order parameter S_b. S_s is defined from the angle between the cell director and the local surface normal, and it varies from 0 for a random configuration to 1 for cells lying parallel to the interface. To characterize the ordering *in* the plane locally tangential to the interface, we make an analogy between biofilm architecture and the arrangement of molecules on the surface of a LC droplet. In the latter case, Boojum points (+1 defects) are observed at two poles (*17*), from which molecules emanate radially and follow the lines of constant longitude, i.e. meridians. Thus, we use the bipolar order parameter S_b to quantify how cells align with the local meridian.

bioRxiv preprint doi: https://doi.org/10.1101/2021.02.17.431682; this version posted February 17, 2021. The copyright holder for this preprint (which was not certified by peer review) is the author/funder. All rights reserved. No reuse allowed without permission.

We average S_s and S_b over cells in the two outmost layers to characterize global cell ordering near the interface. We follow the time evolution of $\overline{S_s}$ and $\overline{S_b}$ (**Fig. 3A**). As embedded biofilms develop, both $\overline{S_s}$ and $\overline{S_b}$ increase steadily with biofilm volume, indicating a gradual self-organization process. Interestingly, the increase in cell ordering is tightly coupled to the global morphological transition. Late in Stage I, accumulating pressure from biofilm expansion favors tangential alignment of cells at the biofilm-gel interface, leading to a fast increase in $\overline{S_s}$. In contrast, $\overline{S_b}$ starts to increase only after $\overline{S_s}$ reaches a value ~0.5. We therefore conclude that shell ordering is a prerequisite for bipolar ordering. Bipolar ordering does not develop until the biofilm enters Stage II in which its oblate shape geometrically defines two poles.

The interior of an embedded biofilm is much less ordered (**Fig. 3B**). However, we do observe a tendency for cells in the core to lie at an average angle of 20° with respect to the principal plane of the biofilm (**Fig. 3B, inset**). Interestingly, there is no preferred orientation within that plane, indicating that cells in the interior are shielded from the shell ordering at the biofilm-gel interface (fig. S13).

Cell ordering is promoted by mechanical interactions across the biofilm-environment interface

We further investigate the dependence of cell ordering on gel stiffness (**Fig. 3C** and fig. 14A). The azimuthally averaged cell orientation (**Fig. 3C, *Bottom***) shows that both the bipolar organization of cells at the biofilm-gel interface and the planar arrangement at the biofilm core become more pronounced as the gel stiffness increases. Two factors underlie the disordered configuration for biofilms grown in low concentration gel (<1%). First, due to the large pore size of these gels (*29*), cells at the biofilm-gel interface are not necessarily tangential to the interface. Second, biofilms grown in low concentration gels experience weaker compression as evidenced by their lower cellular density (fig. S2D). Under these conditions, both $\overline{S_s}$ and $\overline{S_b}$ remain low. As the gel concentration increases, its stiffness increases and so does the mechanical resistance experienced by the embedded biofilm. Accordingly, biofilm cell density increases, and the biofilm shape becomes oblate. The concomitant increase in $\overline{S_b}$ suggests that mechanical stress plays a critical role in cell ordering in confined biofilms (**Fig. 3D**).

bioRxiv preprint doi: https://doi.org/10.1101/2021.02.17.431682; this version posted February 17, 2021. The copyright holder for this preprint (which was not certified by peer review) is the author/funder. All rights reserved. No reuse allowed without permission.

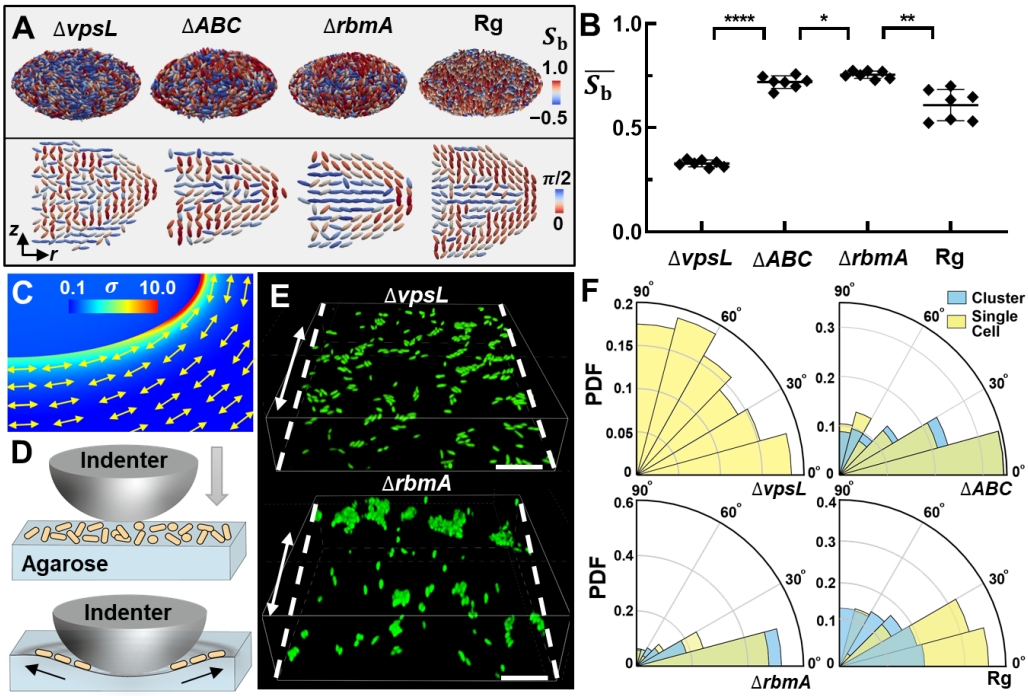

Figure 4. Stress transmission across the biofilm-gel interface by matrix components causes cell ordering. (**A**) Architecture of mature biofilms from different mutants growing inside 2% agarose gels. The same color codes are used as in **Fig. 3D**. Shown from left to right are the biofilms from Δ*vpsL*, Δ*rbmA*Δ*bap1*Δ*rbmC* (Δ*ABC*), Δ*rbmA*, and rugose wild-type (Rg) cells. (**B**) Average bipolar ordering $\overline{S_b}$ calculated for each mutant biofilm. Unpaired *t*-test is performed for statistical analysis; *P< 0.05; **P< 0.01; and ****P< 0.0001; error bars indicate SDs (n = 7). (**C**) Finite element simulation result for the normalized von Mises stress field (σ/G_b) generated by inclusion growth with $\Delta V/V_0 = 25$. Double-headed arrows indicate the local directions of the first principal tensile stress in the gel. (**D**) Schematic illustration of the *in vitro* stress transmission experiment. A spherical indenter generates a radially symmetric deformation field in the agarose gel, whose surface is colonized by randomly oriented cells (yellow cylinders) and small clusters. After indentation, we record the orientation of cells in areas not in physical contact with the indenter. (**E**) Images of single cells and clusters of Δ*vpsL* and Δ*rbmA* mutant cells on the deformed agarose surface stretched along the direction of dashed line. Scale bar: 10 μm. (**F**) Probability distribution function (PDF) of the angles between the axis of cell orientation and the axis of substrate stretching (black arrow in **D**) for different mutants. Yellow corresponds to single cells and blue corresponds to cells in clusters.

Extracellular matrix mediates cell ordering by transmitting stress from the environment

Previous studies on biofilms growing on rigid substrates have shown that cell ordering depends critically on cell-to-surface adhesion, mediated by VPS and accessory proteins RbmC and Bap1 (*9*, *21*, *30*, *31*). We hypothesize that these matrix components also contribute to the cell ordering in embedded biofilms. To test this hypothesis, we generate mutants lacking one or more matrix components (**Fig. 4, A** and **B**) (*26*). We observe that the Δ*vpsL* mutant cluster maintains significant shell order (**Fig. 4A** and fig. S14B), suggesting that the tendency of cells to align tangentially to the biofilm-gel interface is a generic result of confinement and independent of the biofilm matrix. However, Δ*vpsL* cells at the biofilm-gel interface fail to align

bioRxiv preprint doi: https://doi.org/10.1101/2021.02.17.431682; this version posted February 17, 2021. The copyright holder for this preprint (which was not certified by peer review) is the author/funder. All rights reserved. No reuse allowed without permission.

in a bipolar order, and the biofilm core remains disordered. The Δ*rbmA*Δ*bap1*Δ*rbmC* (Δ*ABC*) mutant produces VPS but no accessory proteins; it shows emergent bipolar order near the biofilm-gel interface, but the interior remains disordered. When the surface adhesion proteins are present as in the Δ*rbmA* mutant, cell ordering is fully established (**Fig. 4, A** and **B** and fig. S14). Interestingly, in the Rg biofilms that produce all matrix components (*30*), the bipolar surface order is slightly lower (**Fig. 4B**), and the planar cell ordering at the core is less pronounced (fig. S15). These results confirm the role of VPS and matrix proteins in mediating cell ordering in embedded biofilms.

How do the molecular-scale interactions mediated by these proteins translate into community-scale organization? A hint is given by finite element simulation (**Fig. 4C**). Due to the volumetric expansion of the biofilm, the gel material near the interface experiences large *tensile* stresses. Importantly, the direction of tensile stresses coincides with the direction of cell alignment. Therefore, we hypothesize that cells at the biofilm-gel interface align with the tensile stresses in the gel, and that this stress transmission depends critically on the biofilm matrix. To test this hypothesis, we design an *in vitro* indentation experiment to capture the essence of the mechanical response at the biofilm-gel interface (**Fig. 4D**). We use a spherical indenter to deform the agarose substrate, generating radial tensile stress. In this experiment, the bulk compressive stress from the confining environment is absent so that we can focus on how bacteria respond to the tensile stress in the substrate, either as individual cells or as a collective. To this end, immediately after indentation, we measure the orientations of isolated cells and cells in small clusters that are randomly attached to the surface (**Fig. 4E**). We calculate the distribution of the angle between the axis of cell orientation and that of the local tensile stress in the substrate (**Fig. 4F**). We find that Δ*vpsL* cells maintain a random orientation, suggesting that in the absence of VPS, *V. cholerae* cells are not able to respond to external stress. This observation explains the disordered organization of the Δ*vpsL* biofilm. On the other hand, the Δ*ABC* cells readily align with the tensile stress direction, consistent with the emergence of bipolar order in Δ*ABC* biofilms. Interestingly, this result indicates that VPS, while not sufficient to maintain biofilm-surface adhesion (*9*), can nevertheless transmit stress across the biofilm-gel interface. Similar reorientation dynamics is observed in the Δ*rbmA* mutant, and the degree of alignment is stronger than that in the Δ*ABC* mutant. This is consistent with the stronger ordering observed in the Δ*rbmA* biofilm.

A distinct pattern is observed for the Rg strain in the indentation experiment. Isolated cells on the gel surface readily align with the tensile stress similar to the Δ*rbmA* or Δ*ABC* mutant. However, this mechanical response diminishes significantly in clusters – Rg cells in clusters are nearly randomly oriented and unresponsive to the tensile stress in the substrate. We infer that the cell-to-cell adhesion conferred by RbmA inhibits the reorientation process (*32*) – it may be difficult for mutually adhered cells to reorient collectively (*8*). The impaired alignment with external stress underlies the decreased bipolar order in the embedded Rg biofilms (fig. S15). To sum up, the *in vitro* indentation experiment provides direct evidence that *V. cholerae* cells can align with tensile stress in an adjacent elastic substrate, and that this response depends critically on the matrix components. The bipolar organization of cells in embedded biofilms is a consequence of this alignment to the tangential tensile stress in the gel.

bioRxiv preprint doi: https://doi.org/10.1101/2021.02.17.431682; this version posted February 17, 2021. The copyright holder for this preprint (which was not certified by peer review) is the author/funder. All rights reserved. No reuse allowed without permission.

Outlook

Our results provide a systematic analysis of how bacterial biofilms interact with their mechanical environment: Both the overall morphological evolution and the bipolar cellular organization are distinct features of embedded biofilms and direct consequences of the growth-induced mechanical stresses generated and experienced by confined biofilms. The morphogenetic principles of confined biofilms revealed here are generally applicable to other biofilms and potentially to higher-order organisms developing in mechanically constrained environments (*33*). Our model also describes the generic process of how one solid expands inside another solid – a scenario widely found in the gut microbiome (*34*), organoid development (*35*), tumor growth (*13*) alloy formation (*36*), etc. This work also opens up many interesting directions for future biofilm studies, such as the enhanced resistance of embedded biofilms (fig. S16) to antibiotics and phages. An important question remains in the current system as to whether the observed cell ordering can actively drive changes in biofilm morphology, thus affecting the developmental pathways of the embedded biofilms – treating the growing biofilm as a 3D active nematic medium might shed light on this intriguing possibility (*10*, *37–39*).

bioRxiv preprint doi: https://doi.org/10.1101/2021.02.17.431682; this version posted February 17, 2021. The copyright holder for this preprint (which was not certified by peer review) is the author/funder. All rights reserved. No reuse allowed without permission.

References and Notes

1. K. H. Vining, D. J. Mooney, *Nat. Rev. Mol. Cell Biol.* **18**, 728–742 (2017).

2. G. A. Stooke-Vaughan, O. Campàs, *Curr. Opin. Genet. Dev*. **51**, 111–119 (2018).

3. D. E. Discher, P. Janmey, Y. Wang, *Science*. **310**, 1139–1143 (2005).

4. H. C. Flemming, J. Wingender, *Nat. Rev. Microbiol.* **8**, 623–633 (2010).

5. L. Hall Stoodley, J. W. Costerton, P. Stoodley, *Nat. Rev. Microbiol.* **2**, 95–108 (2004).

6. S. Mukherjee, B. L. Bassler, *Nat. Rev. Microbiol.* **17**, 371–382 (2019).

7. Y. F. Dufrêne, A. Persat, *Nat. Rev. Microbiol.* **18**, 227–240 (2020).

8. B. Qin *et al.*, *Science*. **369**, 71–77 (2020).

9. J. Yan, A. G. Sharo, H. A. Stone, N. S. Wingreen, B. L. Bassler, *Proc. Natl. Acad. Sci. USA*. **113**, E5337–E5343 (2016).

10. R. Hartmann *et al.*, *Nat. Phys.* **15**, 251–256 (2019).

11. T. Bjarnsholt *et al.*, *Pediatr. Pulmonol.* **44**, 547–558 (2009).

12. A. L. Gallego-Hernandez *et al.*, *Proc. Natl. Acad. Sci. USA*. **117**, 11010–11017 (2020).

13. G. Helmlinger, P. A. Netti, H. C. Lichtenbeld, R. J. Melder, R. K. Jain, *Nat. Biotechnol.* **15**, 778–783 (1997).

14. K. D. Irvine, B. I. Shraiman, *Development*. **144**, 4238–4248 (2017).

15. J. K. Teschler *et al.*, *Nat. Rev. Microbiol.* **13**, 255–268 (2015).

16. E. J. Nelson, J. B. Harris, J. G. J. Morris, S. B. Calderwood, A. Camilli, *Nat. Rev. Microbiol.* **7**, 693–702 (2009).

17. I. H. Lin *et al.*, *Science*. **332**, 1297–1300 (2011).

18. Y. G. Jung, J. Choi, S.-K. Kim, J.-H. Lee, S. Kwon, *Appl. Environ. Microbiol.* **81**, 211–219 (2015).

19. R. S. Eriksen, S. L. Svenningsen, K. Sneppen, N. Mitarai, *Proc. Natl. Acad. Sci. USA*. **115**, 337–342 (2018).

20. S. Beyhan, F. H. Yildiz, *Mol. Microbiol.* **63**, 995–1007 (2007).

21. F. Beroz *et al.*, *Nat. Phys.* **14**, 954–960 (2018).

bioRxiv preprint doi: https://doi.org/10.1101/2021.02.17.431682; this version posted February 17, 2021. The copyright holder for this preprint (which was not certified by peer review) is the author/funder. All rights reserved. No reuse allowed without permission.

22. D. Andrienko, *J. Mol. Liq.* **267**, 520–541 (2018).

23. S. Raayai Ardakani, Z. Chen, D. R. Earl, T. Cohen, *Soft Matter*. **15**, 381–392 (2019).

24. S. Kundu, A. J. Crosby, *Soft Matter*. **5**, 3963–3968 (2009).

25. M. Kothari, T. Cohen, *J. Mech. Phys. Solids*. **145**, 104153 (2020).

26. J. Yan *et al.*, *Adv. Mater.* **30**, 1804153 (2018).

27. J. Y. Kim *et al.*, *Sci. Adv.* **6**, eaaz0418 (2020).

28. J. Li, M. Kothari, T. Henzel, S. Cockalingam, Q. Zhang, X. Li, J. Yan, T. Cohen, Nonlinear inclusion theory: Morphogenesis of a confined body, *Manuscript in preparation.*

29. J. Narayanan *et al., J. Phys.: Conf. Ser.* **28**, 83-86 (2006).

30. V. Berk *et al.*, *Science*. **337**, 236–239 (2012).

31. C. Absalon, K. Van Dellen, P. I. Watnick, *PLoS Pathog.* **7**, e1002210 (2011).

32. J. C. Fong *et al.*, *eLife*. **6**, e1002210 (2017).

33. B. Ladoux, R.-M. Mège, *Nat. Rev. Mol. Cell Biol.* **18**, 743–757 (2017).

34. W. R. Whitaker, E. S. Shepherd, J. L. Sonnenburg, *Cell*. **169**, 538-546 (2017).

35. E. Garreta *et al.*, *Nat. Mater.* **20**, 145–155 (2021).

36. F. R. N. Nabarro, *Proc. Phys. Soc.* **52**, 90–93 (1940).

37. K. Copenhagen, R. Alert, N. S. Wingreen, J. W. Shaevitz, *Nat. Phys.* **17**, 211–215 (2021).

38. D. Dell'Arciprete *et al.*, *Nat. Commun.* **9**, 4190 (2018).

39. G. Duclos *et al.*, *Science*. **367**, 1120–1124 (2020).

bioRxiv preprint doi: https://doi.org/10.1101/2021.02.17.431682; this version posted February 17, 2021. The copyright holder for this preprint (which was not certified by peer review) is the author/funder. All rights reserved. No reuse allowed without permission.

Acknowledgments

We thank Drs. A. Mashruwala and N. Høyland-Kroghsbo for their help in the initial experiments. We thank Drs S. Mao, A. Crosby, E. Dufrense, and J.-S. Tai for helpful discussions. **Fundings**: T.C. acknowledges the support of Dr. Timothy B. Bentley, Office of Naval Research Program Manager, under award number N00014-20-1-2561, and support from the National Science Foundation under award number 1942016. R.A. acknowledges support from the Human Frontier Science Program (LT000475/2018-C). J.Y. holds a Career Award at the Scientific Interface from the Burroughs Wellcome Fund. **Author contributions**: Q.Z. and J.Y. designed and performed the experiments. J.L., M.K. and T.C. performed modeling. J.Y. performed strain cloning. Q.Z., H.L., J.N., and J.Y. analyzed the data. Q.Z., J.L., R. A., T.C. and J.Y. wrote the paper.

Data and materials availability

Matlab codes for single-cell segmentation are available online at Github: https://github.com/Haoran-Lu/Segmentation_3D-processing/releases/tag/v1.0. Other data are available upon request.

Competing interests

The authors declare no competing interests.